

# Effect of Potential Field on Ion Deflection and Shape Evolution of Trenches during Plasma-Assisted Etching

Demetre J. Economou<sup>\*,1</sup> and Richard C. Alkire<sup>\*</sup>

Department of Chemical Engineering, University of Illinois, Urbana, Illinois 61801

## ABSTRACT

A mathematical model was developed to study shape evolution of trenches during plasma-assisted etching. A two-region sheath model was used to determine the effect of local potential distribution on ion deflection and on the ion flux and energy distribution along the walls of the trench. The potential field in the near-trench region was found by using the boundary integral method which, coupled with a moving boundary scheme, allowed the time evolution of etch profiles to be computed. The effect of important variables affecting ion deflection and sidewall etching was combined in a dimensionless group  $\Omega$ . For values of  $\Omega \leq 0.1$  and for positive mask potentials, less than 10% of the bombarding ion flux struck the sidewall of a rectangular trench. Ion deflection and ion-neutral collisions resulted in sidewall "bowing" and in decreasing etch rate as a function of trench depth. Such phenomena are especially important in applications which require the etching of deep trenches.

Attainment of anisotropy is an important driving force behind implementation of plasma-assisted etching techniques in semiconductor processing. Anisotropy is promoted when ions gain directionality from the plasma sheath electric field and are accelerated toward the etch feature, thus enhancing the vertical etch rate by preferential bombardment of the bottom surface. We call this "ion-assisted etching." On the other hand, isotropic etching, which leads to undercutting, is commonly associated with the presence of neutral etchant species which, lacking directionality in motion, etch both the sidewalls as well as the bottom of the feature. We call this "chemical etching." The degree of etch anisotropy is thus often said to depend upon the relative importance of ion-assisted etching as compared to chemical etching.

However, sidewall etching can occur even in the absence of chemical etching because of distortion of the electric field in the vicinity of the feature owing to its topography and state of surface charge. Such distortion serves to deflect on-coming ions toward the sidewalls and thus affect adversely the desired anisotropy. The purpose of this investigation was to consider theoretically the phenomenon of ion deflection, particularly in the creation of deep trenches where significant shape evolution occurs during the course of etching.

Deep silicon trenches are used as trench capacitors in high density MOS-DRAM cells and for isolation in high speed bipolar devices (1). High aspect ratio grooves are of importance in trilevel resist processing (2), in a variety of device applications (3), and in advanced three-dimensional integrated circuits. Nanometer-scale high-aspect-ratio trenches may be useful in the fabrication of novel electronic and optoelectronic devices (4). The above applications demand high etch rate while placing severe requirements on the trench wall profile and on wall surface quality. For example, bottle-shaped wall profiles in silicon trenches are unacceptable for subsequent dielectric refilling because such shapes are prone to void formation and device failure. It is therefore worthwhile to investigate phenomena affecting the shape of wall profiles in deep trenches and how this shape evolves during etching.

Ion deflection recently has been suggested as the explanation for observations in a variety of situations. Chin *et al.* (5) observed "bottle-shaped" wall profiles in deep trenches created by reactive ion etching in polysilicon with use of SiO<sub>2</sub> masks. Sidewall "bow" formation was more pronounced for higher aspect ratio trenches, and the etch rate was observed to decrease with increasing trench depth. The authors attributed the observed phenomena to ion deflection due to locally nonuniform electric fields. Bruce and Reinberg (6) investigated the effect of a positive dc bias applied to the RF-driven electrode during Cl<sub>2</sub>/Si etching. The effect of bias, which dramatically affected

etch rate and etch profiles, was attributed to charging of the insulator mask and thus to establishment of local electric fields which deflected oncoming ions toward the exposed silicon surface. Similar effects were also observed by Fung *et al.* (7) in the Si/SF<sub>6</sub> system. In another situation, Gokan *et al.* (8) observed curved sidewalls in photoresist trenches made during oxygen reactive ion beam etching; by increasing the ion bombardment energy, vertical sidewalls were obtained under otherwise identical conditions. Sidewall "bow" formation was also observed by Pogge *et al.* (9) in etching high aspect ratio silicon grooves in a Cl<sub>2</sub>/Ar plasma. Ukai and Hanazawa (10) observed a pattern-width dependence of the degree of lateral etching and attributed it to the sheath electric field distortion by the surface topography, resulting in deflection of incident ions. The potential distribution on dielectric films exposed to charged particle beams has been investigated both experimentally and theoretically (11-14).

Thus it appears that the ion deflection phenomenon influences behavior in many systems, especially when etching deep trenches or when conditions favor dielectric mask charging. However, no quantitative analysis is available to clarify general conditions under which the phenomenon is important or to define scaling parameters which might guide the design of etching systems.

Theoretical simulation of shape evolution of etching features has been carried out for a number of processes including reactive ion etching (15), ion milling, sputtering (16), and plasma etching (17). These studies have led to the "string model" algorithm, a welcome semi-empirical tool for evaluating shape evolution processes. However, some fundamental physical phenomena are not considered explicitly, including potential field phenomena.

The purpose of this investigation was to develop improved methods for calculating the shape evolution of etching trenches based upon the fundamental physical and chemical principles of the phenomena involved.

## Theoretical

An analysis of shape evolution requires detailed evaluation of potential field phenomena, mask charging, gas-phase ion scattering, and surface reaction processes. The theoretical model described below computes the drift velocity of ions transported through the sheath, determines the potential field near the etch site and along the mask surface, determines the trajectory of ionic species in the trench region, and expresses the surface reaction rate as a function of the local ion flux, ion bombardment energy, and concentration of reactive neutral species. In order to track the shape evolution of a trench, the boundary integral method and a moving boundary scheme were employed in a time-sequence of numerical calculations.

Because rigorous calculations are cumbersome and often not essential for clarifying the main features of behavior, a number of simplifications have been introduced.

\*Electrochemical Society Active Member.

<sup>1</sup>Present address: Chemical Engineering Department, University of Houston, Houston, Texas 77004.

These are justified in the text below where they are introduced.

**Dielectric mask charging.**—Charging of a dielectric mask near the feature to be etched is considered first since the potential distribution along the mask will affect the electric field in the near-trench region. Figure 1 illustrates a masking layer on a grounded substrate. The system is irradiated by a uniform current flux  $I_i$ , which is constant, independent of the potential of the surface. (This implies that surface potential buildup is small compared to the energy of the incident beam.) In view of the low ion energies commonly encountered ( $\sim 100$  eV), secondary electron emission is neglected. If the mask potential is positive, any secondaries will be attracted back to the mask. Current can flow from the mask to the substrate by bulk conduction  $I_b$  or by surface conduction  $I_s$ . By assuming a thin mask ( $h \ll l$ ) so that a one dimensional model is applicable, the charge balance equation reads

$$\frac{\partial q}{\partial t} = I_i - \sigma_b \frac{V}{h} + \sigma_s \frac{\partial^2 V}{\partial x^2} \quad [1]$$

The left-hand side of Eq. [1] describes charge accumulation. The second term on the right-hand side of Eq. [1] is conduction current through the bulk. The third term describes surface conduction of current. The charge density is found from Gauss' law

$$q = \epsilon \epsilon_0 \frac{V}{h} \quad [2]$$

Under conditions typical of plasma etching applications, bulk conduction can be neglected as compared to surface conduction. Then, combining Eq. [1] and [2], and introducing the dimensionless variables

$$V^* = \frac{V}{V_0}, \quad x^* = \frac{x}{l}, \quad \tau = \frac{t}{t_0}, \quad t_0 = \frac{\epsilon \epsilon_0 l^2}{h \sigma_s} \quad [3]$$

yields

$$\frac{\partial V^*}{\partial \tau} = \frac{I_i l^2}{V_0 \sigma_s} + \frac{\partial^2 V^*}{\partial x^{*2}} \quad [4]$$

where  $V_0$  is a reference potential. The boundary conditions are taken as

$$V^*(\pm 1, \tau) = 0, \quad V^*(x^*, 0) = 0, \quad \left. \frac{\partial V^*(x^*, \tau)}{\partial x^*} \right|_{x^*=0} = 0 \quad [5]$$

Parameter  $t_0$  is the time scale for charge "leakage" to the substrate by surface conduction. For typical parameter values (CVD  $\text{SiO}_2$ ,  $\sigma_s = 5 \times 10^{-5}$  mho (18),  $h = 10^{-5}$  cm,  $l = 10^{-4}$  cm) one finds  $t_0 \approx 0.1$ s. In an RF plasma reactor,  $I_i$  will be a function of time. In a capacitively coupled reactor with no direct connection to ground, the sheath potential is such that  $I_i$  is a positive ion current over most of an RF cycle. Electron current flows only for a very small fraction of the cycle so as to neutralize the positive ion current, re-

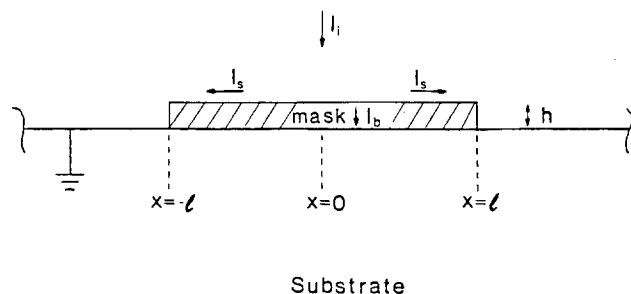


Fig. 1. Definition of coordinate system and flow of current during charging of a masking film.

sulting in zero net current to the surface at the completion of the cycle. Since the time scale of the typical 13.56 MHz frequency is  $t_f = 73.7$  ns  $\ll t_0$ , charge leakage by surface conduction can be neglected on time scale  $t_f$ . Under such conditions, the second term on the right-hand side of Eq. [4] can also be neglected, i.e., all current through the mask is displacement current and the mask acts as a simple capacitor. The simplified form of Eq. [4] written in dimensional units is

$$\frac{dV}{dt} = \frac{I_i h}{\epsilon \epsilon_0} \quad [6]$$

Equation [6] implies that the surface potential is spatially uniform to the extent that  $I_i$  is. In order to estimate the maximum potential the mask will attain in this case, it may be assumed that  $I_i$  is a positive ion current flowing for the whole period of the RF cycle. Then

$$V_{\max} = \frac{I_i h}{f \epsilon \epsilon_0} \quad [7]$$

For typical parameter values one finds  $V_{\max} = 0.1$ V. Charging will be more important at lower frequency. For example, the corresponding figure at  $f = 100$  kHz is  $V_{\max} = 10$ V.

However, the situation is different when an external bias voltage is dc coupled to the electrode. For example, if the wafer is resting on the grounded electrode and a positive dc bias is applied to the RF electrode in a diode reactor, a net positive charge will flow towards the wafer. In this case net charge flow takes place over times long compared to  $t_0$ . Therefore, the full Eq. [4] must be used. Taking a constant time-average value of  $I_i$  for simplicity, one obtains the solution of Eq. [4] as (19)

$$V^*(x^*, \tau) = \frac{A_0}{2} \left\{ 1 - (x^*)^2 - \frac{32}{\pi^3} \sum_{n=0}^{\infty} \frac{(-1)^n}{(2n+1)^3} \cos \frac{(2n+1)\pi x^*}{2} \exp \left( -\frac{(2n+1)^2 \pi^2 \tau}{4} \right) \right\} \quad [8]$$

where

$$A_0 = \frac{I_i l^2}{V_0 \sigma_s} \quad [9]$$

The steady-state potential distribution is found from Eq. [8] by letting  $\tau \rightarrow \infty$ . The result is a quadratic distribution

$$V_{ss}^*(x^*) = \frac{A_0}{2} [1 - (x^*)^2] \quad [10]$$

A quadratic potential distribution was experimentally obtained by Yochizawa *et al.* (20) on the surface of a  $\text{SiO}_2$  film bombarded by positive ions during ion implantation.

**The two-region sheath model and potential distribution in the near-trench region.**—A two-dimensional etching trench model is now considered (21). Surface features are shown in Fig. 2 to be separated from the plasma by the sheath. Ions formed in the plasma drift to the plasma-sheath interface and enter the sheath where they gain energy from the electric field force. In regions some distance from the surface, the field lines are not affected by the surface topography and are thus normal to the macroscopic surface, i.e., the potential distribution is one dimensional. However, in the vicinity of the features, the field lines are distorted and the potential distribution is two dimensional. The distortion of the field lines gives rise to lateral field components that can affect the trajectory of oncoming ions. In principle, the electric field attains an infinitely large value at the sharp corner of the mask. In order to decouple the effect of collisions from the two dimensionality of the electric field, the sheath is divided into two subregions as shown in Fig. 2 (not drawn to scale): (a)

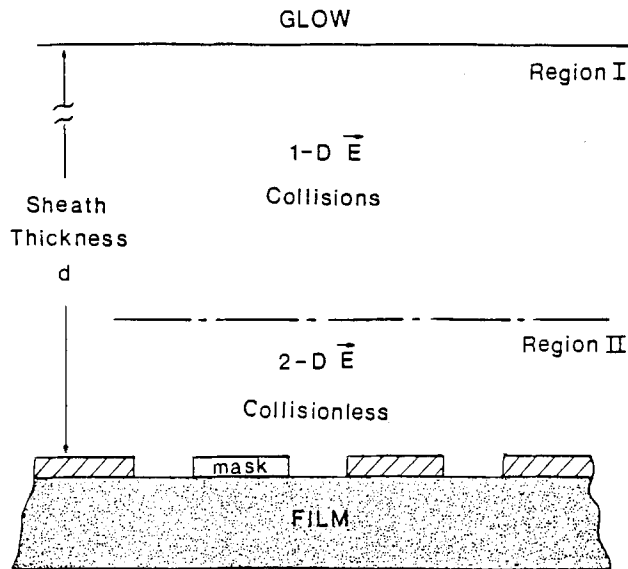


Fig. 2. Surface features and division of sheath into two regions. (not drawn to scale).

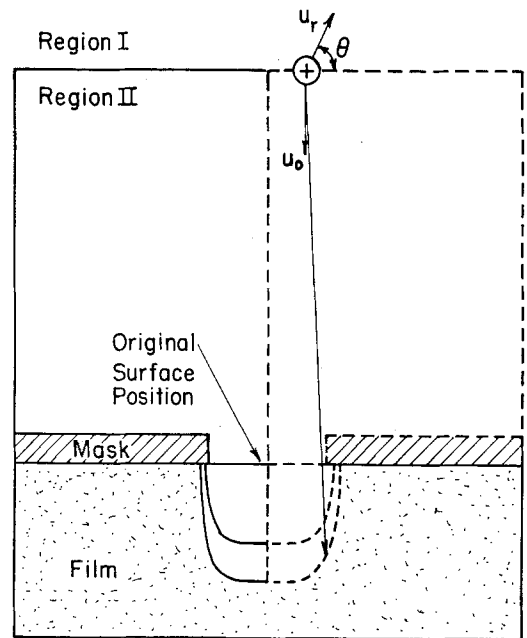
Region I some distance from the surface where the potential field is one dimensional and where ions can experience collisions; and (b) a collision-free Region II near the surface where the potential field is two dimensional owing to the surface topography. For typical trench dimensions, Region II is expected to be  $\approx 10 \mu\text{m}$  thick. Typical sheaths in RF discharges are a few mm thick. Hence the thickness of Region I is about equal to the sheath thickness. No rigorous procedure was applied for determining the exact thickness of Region II. An approximate procedure was used instead, in which the Region I/II interface was moved far enough from the features so that the potential distribution became essentially one dimensional beyond the interface towards Region I. Such "adjustment" will not affect results in Region I. Nor should Region II be affected provided that the correct boundary condition for the potential is used at the I/II interface.

In Region I ions are accelerated by the one dimensional electric field and collide with neutral species. The ion drift velocity in Region I may be obtained by solving an equivalent dc model of the RF sheath as described elsewhere (22), by considering Poisson's equation for the potential distribution coupled to the ion motion and current continuity equations. Figure 3 depicts an ion at the interface between Regions I and II, and indicates that such an ion has a velocity which includes a directional (drift) component  $u_0$  as well as a random component  $u_r$  arising from collisions the ion suffered in Region I. In the present work, no attempt was made to compute the angular distribution of ions arriving at the interface of Regions I and II. Instead it was assumed that the random velocity component  $u_r$  has a value which is a small fraction of  $u_0$ .

Now consider events in Region II. The plasma is weakly ionized and a typical ion density in the bulk plasma is about  $10^{10}$  ions/cm<sup>3</sup>. Close to the solid surface the ion density falls by about an order of magnitude. Hence there will be for each ion a residence volume of about  $10^3 \mu\text{m}^3$ , corresponding to a cube of  $10 \mu\text{m}$  side. Since the thickness of Region II is typically less than  $10 \mu\text{m}$ , Region II can thus be considered to be essentially devoid of other charged species except for the ion of interest. Therefore the potential distribution in the trench region can be computed by using the Laplace equation. Furthermore, the ionic mean free path is typically larger than  $50 \mu\text{m}$ . Hence Region II is collision-free as well, although the possibility exists of collisions with species coming off the surface in a deep trench.

By referring to Fig. 3 and 4, Laplace's equation reads

$$\frac{\partial^2 \phi}{\partial x^2} + \frac{\partial^2 \phi}{\partial y^2} = 0 \quad [11]$$



--- : Computational Domain

Fig. 3. The near-trench Region II: computational domain and schematic of ion trajectory.

The boundary conditions are

$$\phi = \phi_1 \text{ on } S_1, \quad \frac{\partial \phi}{\partial x} = 0 \text{ on } S_2 \text{ and } S_3, \text{ and } \phi = 0 \text{ on } S_6 \quad [12]$$

where the etching film has been assumed to be grounded. Two cases were considered for the boundary condition at the mask surface: a constant or a quadratic potential

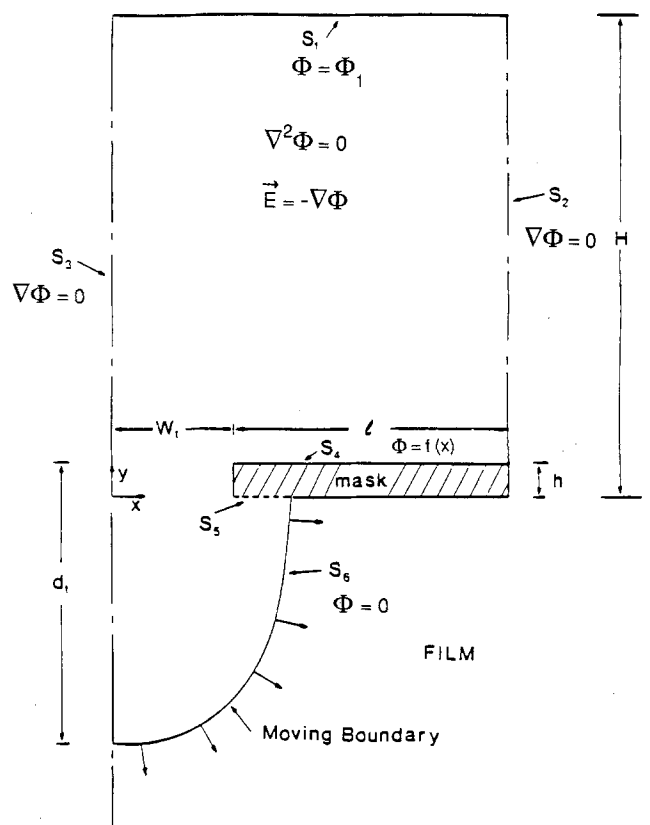


Fig. 4. The near-trench Region II: boundary conditions

$$\phi = \phi_4 = \text{const.} \quad [13a]$$

or

$$\phi = \phi_4 = -\frac{\phi_0}{l^2} [x^2 - 2(w_t + l)x + w_t^2 + 2w_tl] \text{ on } S_4 \quad [13b]$$

where  $x = w_t$  at the left corner of the mask (where  $\phi = 0$ ) and  $x = w_t + l$  at the right symmetry plane (where  $d\phi/dx = 0$ ). In Eq. [13b],  $\phi_0$  is the mask potential at the symmetry plane. A constant mask potential (independent of position on the mask) would be applicable, for example, for a metal mask or for a dielectric mask at high frequencies with no dc bias applied. A quadratic distribution of mask potential would be applicable for a dielectric mask when net current flows to the mask.

Equation [11] was nondimensionalized by defining

$$\Phi = \frac{\phi}{\phi_1}, \quad X = \frac{x}{w_t}, \quad Y = \frac{y}{w_t} \quad [14]$$

whence

$$\frac{\partial^2 \Phi}{\partial X^2} + \frac{\partial^2 \Phi}{\partial Y^2} = 0 \quad [15]$$

$$\Phi = 1 \text{ on } S_1, \quad \frac{\partial \Phi}{\partial X} = 0 \text{ on } S_2 \text{ and } S_3,$$

$$\Phi = \frac{\phi_4}{\phi_1} \text{ on } S_4, \text{ and } \Phi = 0 \text{ on } S_6 \quad [16]$$

The case of an excessive mask undercut (shown in Fig. 4 as surface  $S_5$ ) would invalidate the present analysis. More specifically, the overhanging part of the mask would attain a higher potential since there is no convenient way for current to leak to the substrate. However, etching of deep trenches requires conditions under which ion-assisted processes dominate, in which case etching directly under the mask will be minimal.

*Ion trajectories.*—After the potential distribution in Region II was found by solving Laplace's equation, ion trajectories in Region II were calculated by using the equations of motion, one for each spatial coordinate

$$\frac{d^2x}{dt^2} = \frac{eE_x}{M_+}, \quad \frac{d^2y}{dt^2} = \frac{eE_y}{M_+} \quad [17]$$

The only force acting on the ion was assumed to be the electric field force. Initial conditions included ion position and velocity. By defining dimensionless space coordinates  $X$  and  $Y$  along with a dimensionless time  $T = tu_0/d_t$ , one has

$$\frac{d^2X}{dT^2} = \frac{1}{2} \Omega \left( -\frac{\partial \Phi}{\partial X} \right), \quad \frac{d^2Y}{dT^2} = \frac{1}{2} \Omega \left( -\frac{\partial \Phi}{\partial Y} \right) \quad [18]$$

where the dimensionless ratio

$$\Omega = \left( \frac{d_t}{w_t} \right)^2 \frac{e\phi_1}{1/2 M_+ u_0^2} \quad [19]$$

appears.  $\Omega$  can also be written in a more general form as

$$\Omega = (\text{trench aspect ratio})^2 \frac{\text{energy imparted to the ion by the field}}{\text{kinetic energy of entering ion}}$$

Because of their momentum, ions do not necessarily follow the bent electric field lines in the near-trench region. The degree of ion "deflection" will depend on  $\Omega$ . The higher the value of  $\Omega$ , the more important ion deflection will be. Thus one expects more sidewall etching for trenches with high aspect ratio (5), and less sidewall etching as ion kinetic energy increases (8). As an example, for electric fields of the order of  $10^3$ - $10^4$  V/cm close to the trench, the energy imparted to an ion by the field over a

distance of travel of say 5  $\mu\text{m}$ , will be 0.5-5 eV. For ions entering with a kinetic energy of say 50 eV, and for a trench aspect ratio of 3,  $\Omega$  will be in the range of 0.1-1.0. However, for shallow trenches, e.g. aspect ratio of 1,  $\Omega$  will be in the range of 0.01-0.1.

*Surface reaction kinetics.*—The total etch rate was assumed to be the sum of two contributions: a chemical etching component ( $R_n$ ) arising from the spontaneous etching of the film by neutrals, and an ion-assisted component ( $R_+$ ) owing to ion bombardment effects

$$R_t = R_n + R_+ \quad [20]$$

The contribution of a third component, sputtering, was neglected in comparison with the other two in this analysis. For deep trench etching, one needs  $R_+ \gg R_n$ . For the chemical etching component, linear kinetics were assumed to apply,  $R_n = k_n C$ , where  $C$  is the neutral etchant concentration. The ion-assisted component was assumed to have a form which is linear in ion flux and energy, and independent of neutral concentration

$$R_+ = k_+ I_+ \epsilon_+ \quad [21]$$

Equation [21] implies that the ion-assisted etching is proportional to the power deposited on the surface by the bombarding ions. The total etch rate was then taken as

$$R_t = k_n C + k_+ I_+ \epsilon_+ \quad [22]$$

The form of Eq. [22] is only tentative and has been discussed elsewhere (23). If knowledge of rate processes is available for specific systems, the appropriate equations could be used in place of Eq. [21] and/or [22].

*The boundary integral method.*—Finite element and boundary integral methods have been found to be particularly amenable to prediction of shape evolution phenomena since, in these methods, piecewise polynomials are used to conform to boundaries of arbitrary shape (24). The boundary integral method (BIM) has the additional advantage of reducing the problem dimensionality. For example, a two dimensional problem becomes reduced to a form involving quantities only on the boundary of the two dimensional domain. In contrast, the finite element method (FEM) would require discretization of the entire domain. However, the BIM has the disadvantage of restricted applicability; in general, the BIM cannot be applied to problems governed by nonlinear equations. Another disadvantage of the BIM as compared to the FEM or even the finite difference method (FDM), is that BIM creates a matrix which is full and asymmetric whereas FEM and FDM generate banded matrices. Nevertheless, boundary element methods are well suited for solving Laplace's equation in arbitrary domains. The solution for the potential at any point of the domain can be obtained as an integral involving the values of the potential and its derivative on the domain boundary only. Approximations are introduced in trying to evaluate the boundary integral numerically. The boundary element method was used in this work to solve Laplace's equation in the deforming domain of an etching trench.

*Method of solution.*—The moving boundary problem of tracking the shape evolution of a microscopic etching feature was solved in a stepwise manner. The computational domain is shown in Fig. 4 where, owing to symmetry, only half of Region II was considered. At each time step, Laplace's equation was solved for given boundary conditions to find the electric field distribution in the near-trench region. The domain boundary was discretized by using linear elements. The element length was smaller around the corner of the mask where larger potential gradients are expected. In all moving boundary calculations, lengths were nondimensionalized with respect to the trench mouth half-width, which was taken as having unit length. Linear interpolating functions were also used for the potential and its derivative. Potential distribution calculations using the BIM agreed with independent calculations using the FEM. After having found the electric field

distribution, the trajectory of ions injected at the interface between Regions I and II was computed by using Eq. [17]. Initial values for ion position along the interface and ion velocity components were specified, and Eq. [17] were integrated by a Runge-Kutta method. Trajectory calculations were performed for a number of ions uniformly distributed along plane  $S_1$ . The distance between adjacent ions was typically 0.001 dimensionless units. The above procedure was thought to be a simulation of a uniform ion flux entering the trench region. Calculations of an ion trajectory stopped when the ion hit either the mask or the etching film. Both the mask and the film were regarded as perfectly absorbing surfaces, i.e., ion reflection was not considered. The symmetry planes were regarded as perfect ion reflectors. The mask was assumed nonerodible so that ions hitting the mask did not have to be further considered. Having found the point and energy upon impact on the surface of each and every ion, the number of ions (and their energies) that struck a given element along the discretized moving boundary was determined. The ion-enhanced etch rate for each element was then found by

$$R_{+j} = k_+ \frac{\sum_{i=1}^{N_j} \epsilon_i}{L_j N_t} \quad [23]$$

where the summation term describes the total energy deposited by ions which struck element  $j$ . Division by  $N_t$  in Eq. [23] ensures that the calculated etch rate is independent of the total number of ions used. Furthermore, division by the element length  $L_j$  is required to express the etch rate in terms of unit area. In this manner the distribution of the ion-enhanced component of etching along the moving boundary was found. Another method to calculate the ion flux distribution on the etching surface is to find the curve  $s = s(b)$ , where  $s$  is the coordinate along the boundary, and  $s(b)$  is the point on the boundary struck by an ion having "impact parameter"  $b$ . In this case  $b$  is the distance from the left symmetry plane of an ion injected at the I/II interface. The ion flux can then be found as proportional to  $(\partial s/\partial b)^{-1}$ .

The chemical etch rate was taken as  $R_{nj} = k_n C = \text{constant}$  for all elements. The total etch rate for each element was the sum of the two components,  $R_j = R_{+j} + R_{nj}$ . Elements were then moved to a new position according to local element etch rates. The new nodal positions were found in terms of the old positions and the local etch rates. Movement of the surface to the new position completed one time step. A sequence of such steps was carried out in order to track the shape evolution of the etching trench.

Control over element size was exercised to avoid errors and instabilities of the moving boundary scheme. If elements were too small they would receive a statistically inadequate number of ions resulting in error in the computed element etch rate. On the other hand, large elements would degrade the accuracy of the potential distribution. To avoid such problems, the nodes of an element whose length was smaller than a preset value were merged into one node, or a midpoint node was inserted into an element whose length was larger than a predetermined size. The time step size for boundary displacement was determined by the etch rate. Faster etch rates required smaller time steps to avoid error accumulation and/or instabilities. Even when precautions were taken, however, instabilities would still occur for some combinations of parameters. Such instabilities were manifested as "spikes" or "ripples," especially on the floor of the trench. Smoothing was applied along the bottom part of the trench by using a cubic spline with variable degree of smoothing capability to ensure that any physically significant features of the surface shape were not arbitrarily suppressed.

Calculations in which potential field effects were disregarded required, under typical conditions (e.g., Fig. 6), about 80s of CPU time on the CDC Cyber 175 machine. When potential field effects were included, each surface contour (such as shown in Fig. 10) required typically 10-35 min (depending on trench depth) of CPU time on the same machine.

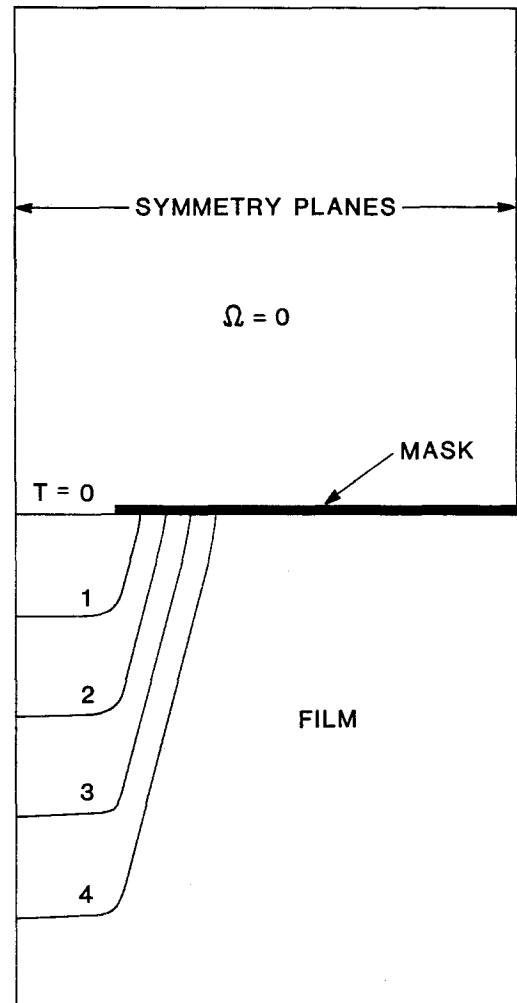


Fig. 5. Shape evolution of a feature under combined chemical and ion-assisted etching. Vertical ion bombardment ( $U_x = 0$ ) and no potential field effects ( $\Omega = 0$ ). Degree of anisotropy is 0.75.

## Results and Discussion

*Shape evolution in the absence of potential field effects.*—The limiting case of no potential field effects on the ion motion in Region II was investigated to test the performance of the computer code, especially the moving boundary computational scheme. Such a situation may be encountered when etching, for example, shallow features at high frequencies without any dc bias applied. Under these conditions ion deflection effects are expected to be minimal.

Figure 5 shows the time evolution of a feature under combined chemical and ion-assisted etching. In this case the assigned degree of anisotropy was equal to 0.75, i.e., ion-assisted etching was three times faster than chemical etching. The uniform ion flux irradiating the surface was assumed to impinge along the vertical. Hence, ion-assisted etching for elements "shadowed" by the mask was set equal to zero. In accordance with expectations, at any time during etching, the extent of mask undercut is equal to one quarter of the etched depth. Many practical systems fall in this category in which some mask undercut is inevitable. An important goal of plasma reactor design is to minimize or eliminate such mask undercut.

The case of ions arriving with a lateral velocity component may be encountered in etching reactors in which the sheath thickness is greater than the ion mean-free-path. Ions will then suffer collisions with neutrals partly randomizing the ion motion. Figure 6 shows the time evolution of the shape of an etching trench for the case of ions entering through the upper plane with a lateral velocity component (along the x-axis) with magnitude equal to 1/10 that of the ion vertical velocity component. The sign of the

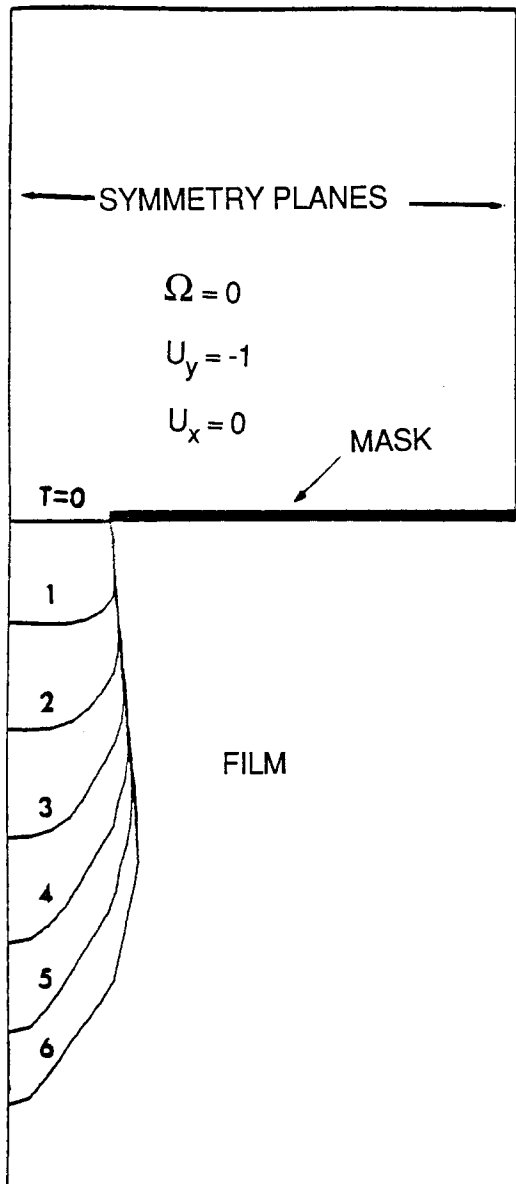


Fig. 6. Shape evolution of a trench under ion-assisted etching only and in the absence of potential field effects ( $\Omega = 0$ ). Entering ion dimensionless velocity components were  $U_{x0} = 0.1$ ,  $U_{y0} = -1$ .

x-velocity component was chosen randomly. Only ion-assisted etching was assumed to occur.

Certain features of the profiles in Fig. 6 are worth noting. First, one observes a widening of the trench owing to ions impinging on the sidewalls. The maximum widening seen in Fig. 6 is 30% of the trench mouth half-width and would further increase if etching was allowed to continue for longer times. Second, the etch rate diminishes as the trench deepens. This is not surprising considering the fact that the entering ion flux remains constant and a larger fraction of the ions are striking the sidewalls as the trench becomes deeper. If the ion velocity were entirely along the vertical, such ions would have been available for etching the bottom of the trench. The etch rate is higher near the symmetry axis because that portion of the trench surface is exposed to a larger ion flux. Finally, no mask undercut is observed, since chemical etching was not allowed to exist and ions cannot strike the surface directly under the mask.

*Potential distribution in the near-trench region and ion deflection effects.*—The potential distribution on a dielectric mask subjected to a uniform ion flux at time zero is described by Eq. [8], the solution of which is shown in Fig. 7. Note that the plot has been displaced by one unit on the x-axis as compared to the coordinate system of Fig. 1. The

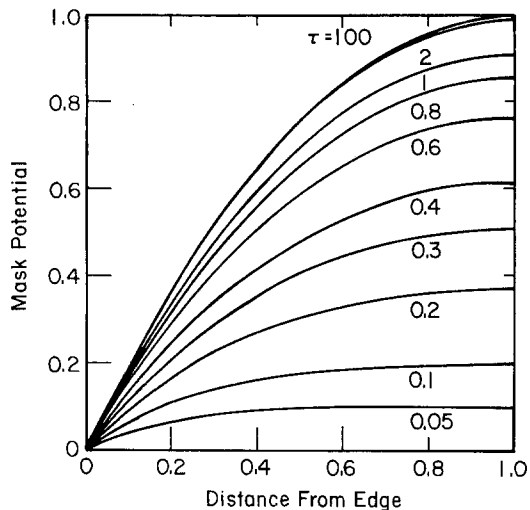


Fig. 7. Dimensionless mask potential as a function of dimensionless position and time.

steady-state potential profile depends on the square of the distance from the mask edge (Eq. [10]) and is attained after a few time constants  $t_0$ . Owing to symmetry, the curves cross the axis  $x = 1$ , at right angles. At any time, the maximum potential occurs at the centerline. The edge potential ( $x = 0$ ) is always zero, since the mask was assumed to be thin compared to its width and in good contact with the underlying substrate held at ground potential. The maximum steady-state potential depends on the level of the incident ion flux and the surface conductivity of the mask (Eq. [9]). High ion currents tend to increase the potential while high surface conductivity acts in the opposite direction.

Figure 8 shows the potential distribution in a 5:1 trench for the case of infinitely small mask thickness and a positive mask potential varying quadratically with distance from the corner (Eq. [13b]). The maximum mask potential at the right symmetry plane was set equal to 0.5 (normal-

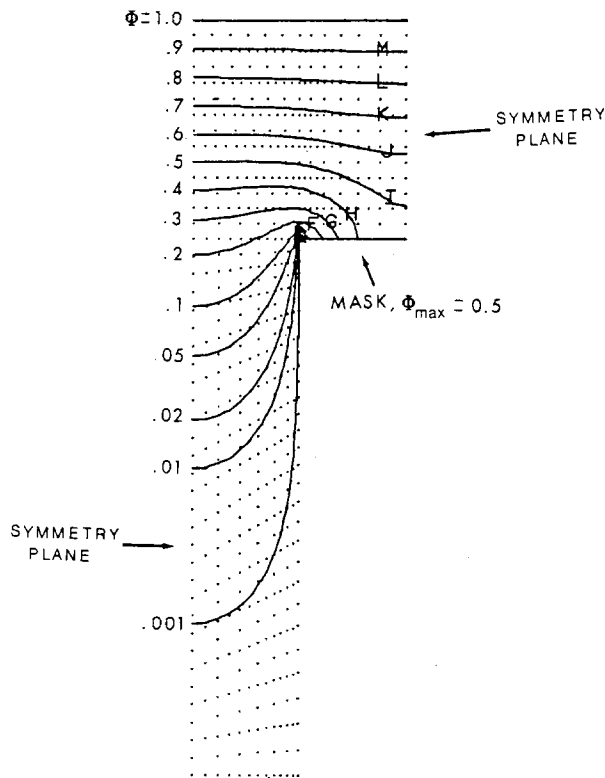


Fig. 8. Potential distribution around a rectangular trench for a quadratic mask potential with  $\Phi_{max} = 0.5$ .

ized with respect to the potential of the upper plane). The electric field right above the mask is such that positive ions experience a lateral force to the left which could redirect oncoming ions toward the trench opening. However, after entering the trench, ions are attracted toward the sidewalls by the image charge induced by the positive-ion/ground-wall combination.

The trajectory of ionic species traversing the near-trench Region II will depend on the potential distribution in that region as well as on the momentum of the incoming ions. Whether or not an ion will strike the sidewall of the trench will also depend on the trench aspect ratio and the position of the entering ion. Determining the ion flux distribution along the walls of an etching trench is of interest since it affects the ion-assisted etch rate distribution. Figure 9 shows a discretized ion flux distribution along the walls of the 5:1 rectangular trench considered in Fig. 8. Ions were assumed to enter with their velocity vector along the vertical, and parameter  $\Omega$  was set equal to unity. Position 0 corresponds to the mask/film interface and position 5 corresponds to the trench bottom corner. The ion flux is low around position 0 because of the repelling action exercised on positive ions flying close to the edge of the positively charged mask. Such ions however are attracted by the sidewall deeper in the trench. The result is a local maximum in the ion flux distribution along the sidewall. The ion flux on the floor of the trench, between positions 5 and 6, is higher than on the sidewalls, since entering ions have all their velocity along the vertical and ions flying at a distance from the mask are not deflected sufficiently to strike the sidewall. Figure 10 shows the fraction of ions hitting the sidewall of the trench considered in Fig. 9, as a function of  $\Omega$ . For  $\Omega \leq 0.1$ , less than 10% of the ions strike the sidewall. For even smaller values of  $\Omega$  ( $<0.01$ ), the ion motion is not significantly perturbed by the lateral electric field. Essentially all ions will then strike the bottom of the trench as long as the ions enter along the vertical. The percentage of ions striking the sidewall increases monotonically with  $\Omega$ . For a given trench aspect ratio, the distribution of ion flux will approach the primary current distribution (19) in the trench as  $\Omega \rightarrow \infty$ . This is because ions have zero momentum in the limit  $\Omega \rightarrow \infty$ , and ions will then follow the electric field lines. Finally, the fraction of ions striking the sidewall is expected to attain a value of nearly 100% as the trench aspect ratio increases indefinitely.

Figure 11 shows the shape evolution of a trench under conditions of ion-assisted etching only. The mask potential was assumed to depend quadratically on distance from the mask edge, attaining a maximum value of 0.5 at the right symmetry plane. The etching surface was at ground potential. Parameter  $\Omega$  was set equal to 1. Although the en-

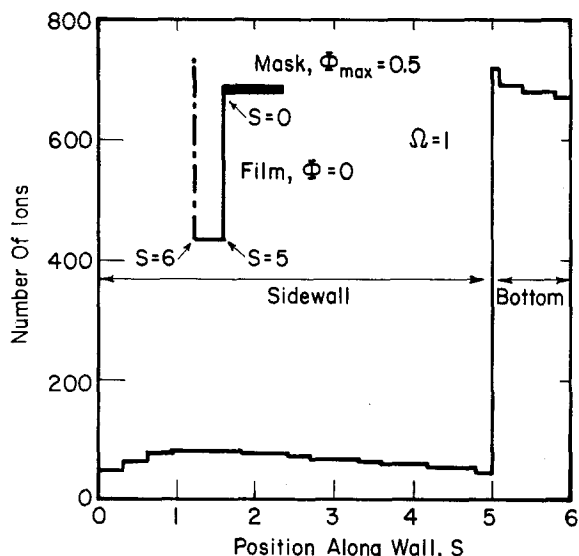


Fig. 9. Ion flux distribution along the walls of a rectangular trench for a quadratic mask potential with  $\Phi_{max} = 0.50$  and for  $\Omega = 1$ .

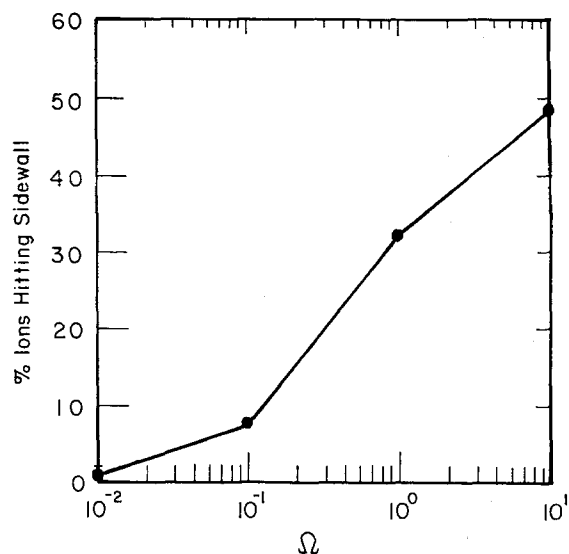


Fig. 10. Fraction of ions hitting sidewall of the trench of Fig. 9 as a function of  $\Omega$ .

tering ions had no lateral velocity component, the diverging action of the field caused a portion of the ion flux to strike the sidewall, resulting in widening of the trench. The maximum widening seen in Fig. 11 is 40% of the trench mouth half-width. In addition, etch rate decreases with depth for the same reason as in Fig. 6.

Sidewall etching and diminishing etch rate as a function of depth have important implications in deep trench etching applications. The phenomena are amplified as the trench becomes deeper and as the lateral ion velocity component increases. Under given etching conditions, deep trenches are expected to attain a limiting depth at which further vertical etching would proceed only very slowly. These are potential problems in the fabrication of advanced nanometer scale devices (25). At long etching times, sidewall "bow" is significant and ions which would otherwise strike the corner sidewall, hit the bottom of the trench. Hence, the portion of the trench floor close to the corner receives comparatively higher ion flux and a slight "trenching" develops as seen in Fig. 11 for  $T = 2.8$ . More-

**Ion-assisted Etching Only**

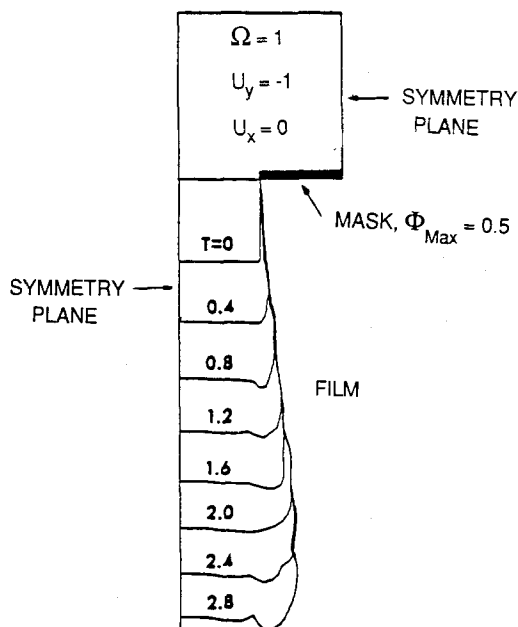


Fig. 11. Shape evolution of a trench under ion-assisted etching only. Entering ion dimensionless velocity components were  $U_{x0} = 0$ ,  $U_{y0} = -1$ . Quadratic mask potential with  $\Phi_{max} = 0.5$ .  $\Omega = 1$ .

over, if ions were allowed to enter the near-trench region with a lateral velocity component, a fraction of the ions would strike the sidewall further up from the trench floor. The resultant sidewall profile would be a combination of the profiles shown in Fig. 6 and 11.

### Summary and Conclusions

A mathematical model was developed to study the effect of local potential distribution on ion deflection and on the resulting shape evolution of trenches during ion-assisted etching.

A dielectric mask charging model showed that, under conditions typical of RF etching discharges, mask charging can be important when a net current flows to the mask, such as under conditions of applied dc bias, or when operating at low plasma excitation frequency. For a positive mask potential, the resultant potential distribution in the near-trench region was such that ions, which would otherwise strike the mask, could be redirected toward the trench opening. The degree of ion deflection depended on the potential distribution around the trench and on the ion kinetic energy. The degree of trench sidewall bombardment also depended on the trench aspect ratio. The effect of these variables was combined in a dimensionless group  $\Omega$ . Ion deflection and sidewall bombardment became more predominant as the value of  $\Omega$  increased. For positive mask potentials and for values of  $\Omega \leq 0.1$ , less than 10% of the impinging ion flux struck the sidewalls of a rectangular trench. Further, ion-neutral collisions which randomize the ion motion and reduce the ion energy rendered ions more susceptible to deflection. These phenomena resulted in trench sidewall "bowing" as the wall profile evolved during etching, as well as decrease of etch rate with trench depth. The phenomena were amplified as trench aspect ratio increased.

Owing to the complexity of the system, simplifying assumptions had to be invoked which limit the parameter range over which the model is applicable. For example, effects of surface microstructure on the ion trajectory, ion collisions within the trench with outcoming reaction products, ion reflection from the surface, time variation of the surface potential, and surface diffusion were not accounted for in this first-generation attempt. Further, cases of dielectric substrate films and the corresponding potential distribution along the surface of the film, or the case of possible mask erosion, were not examined. Improvements in efficiency of the computer code would allow more detailed investigation of parameter effects on etch profiles.

In addition to ion deflection, other phenomena may be important when etching deep trenches. Such phenomena include redeposition of low volatility products, polymer deposition along the trench sidewalls, and reactant and/or product diffusional limitations in very deep trenches.

Experimental data under well controlled conditions are needed to test the model predictions and to make refinements in underlying hypotheses. A relatively "clean" system (e.g., no polymerization) and etching conditions for which ion-assisted processes dominate should be used for such experimental work. The  $\text{Cl}_2$ /undoped-Si system appears to be a good candidate. Measurement of mask surface potential, and of ion energy and flux under conditions of applied bias or without bias, combined with SEM pictures of etched trench profiles would provide a firm data base against which the model predictions could be compared. More carefully characterized experiments could also be performed in an ion-beam etching apparatus.

### Acknowledgments

This work was partially supported by the NSF Engineering Research Center on Compound Semiconductors, and by Grants-in-Aid from Tektronix and IBM.

Manuscript submitted March 20, 1987; revised manuscript received Dec. 23, 1987.

### LIST OF SYMBOLS

#### English Letters

$C$  neutral etchant species concentration,  $\text{mol}/\text{cm}^3$   
 $d_t$  trench depth,  $\text{cm}$

$E$  electric field,  $\text{V}/\text{cm}$   
 $e$  electronic charge,  $1.602 \cdot 10^{-19} \text{ C}$   
 $f$  frequency,  $1/\text{s}$   
 $h$  mask thickness,  $\text{cm}$   
 $I$  current,  $(\text{cm}^2\text{s})^{-1}$  or  $\text{mA}/\text{cm}^2$   
 $k$  Boltzmann constant,  $1.38066 \cdot 10^{-23} \text{ J}/\text{K}$   
 $k_n$  chemical (neutral) etching rate constant,  $\text{cm}/\text{s}$   
 $k_+$  ion-enhanced etching rate constant,  $\text{mol}/\text{eV}$   
 $l$  mask half-width,  $\text{cm}$   
 $L_j$  length of element  $j$ ,  $\text{cm}$   
 $N_t$  total number of ions hitting moving boundary  
 $N_j$  number of ions hitting element  $j$   
 $q$  charge density on mask,  $\text{C}/\text{cm}^2$   
 $R_t$  total etching rate,  $\mu\text{m}/\text{min}$ , or  $\text{mol}/\text{cm}^2\text{s}$   
 $R_n$  chemical etching rate,  $\mu\text{m}/\text{min}$ , or  $\text{mol}/\text{cm}^2\text{s}$   
 $R_+$  ion-enhanced etching rate,  $\mu\text{m}/\text{min}$ , or  $\text{mol}/\text{cm}^2\text{s}$   
 $t$  time,  $\text{s}$   
 $T$  dimensionless time for ion motion in Region II  
 $u_x, u_y$  ion velocities in Region II,  $\text{cm}/\text{s}$   
 $u_o$  ion drift velocity upon entering Region II,  $\text{cm}/\text{s}$   
 $u_r$  ion random velocity upon entering Region II,  $\text{cm}/\text{s}$   
 $U_x, U_y$  dimensionless ion velocities in Region II  
 $V$  potential,  $\text{V}$   
 $w_t$  trench mouth width,  $\text{cm}$   
 $x, y$  cartesian coordinates,  $\text{cm}$   
 $X, Y$  dimensionless cartesian coordinates

#### Greek Letters

$\epsilon_0$  permittivity in vacuum,  $8.85418 \cdot 10^{-14} \text{ F}/\text{cm}$   
 $\epsilon$  mask relative dielectric constant  
 $\epsilon_+$  ion energy,  $\text{eV}$   
 $\tau$  dimensionless time (Eq. [3])  
 $\phi$  potential,  $\text{V}$   
 $\Phi$  dimensionless potential  
 $\Omega$  dimensionless group (Eq. [19])

#### Subscripts

$+$  positive ions  
 $*$  dimensionless quantity

### REFERENCES

1. A. Hayasaka, Y. Tamaki, M. Kawamura, K. Ogiue, and S. Ohwaki, *IEDM Tech. Dig.*, 62 (1982); K. D. Rung, H. Momose, and Y. Nagakubo, *ibid.*, 237 (1982); H. Sunami, T. Kure, N. Hashimoto, K. Itoh, T. Toyabe, and S. Asai, *ibid.*, 806 (1982).
2. J. Kruger, M. O'Toole, and P. Rissman, in "VLSI Electronics: Microstructure Science," Vol. 8, N. Einspruch and D. Brown, Editors, Academic Press (1984).
3. D. L. Kendall, *Annu. Rev. Mater. Sci.*, 9, 373 (1979).
4. R. E. Howard, *Mat. Res. Soc. Symp. Proc.*, 38, 247 (1985).
5. D. Chin, S. H. Dhong, and G. J. Long, *This Journal*, 132, 1705 (1985).
6. R. H. Bruce and A. R. Reinberg, *ibid.*, 129, 393 (1982).
7. C. D. Fung, C. Y. Tung, and W. H. Ko, Abstract 402, p. 578, The Electrochemical Society Extended Abstracts, Vol. 84-2, New Orleans, LA, Oct. 7-12, 1984.
8. H. Gokan, M. Itoh, and S. Esho, *J. Vac. Sci. Technol.*, B2, 34 (1984).
9. H. B. Pogge, J. A. Bondur, and P. J. Burkhardt, *This Journal*, 130, 1592 (1983).
10. K. Ukai and K. Hanazawa, *J. Vac. Sci. Technol.*, A2, 464 (1978).
11. J. Robinson and N. Quoc-Nguyen, *IEEE Trans. Electr. Insul.*, EI-14, 14 (1979).
12. J. Stevens, C. Purvis, and J. Staskes, *IEEE*, NS-25, 1304 (1978).
13. C. Purvis, N. Stevens, and J. Oglebay, in "Proceedings of Spacecraft Charging Technology Conference," C. P. Pike and R. R. Lovell, Editors, p. 459-486, NASA TMX 73537/AFGL TR-77-0051 (1977).
14. R. D. Reeves and K. G. Balmain, *IEEE*, NS-28, 4547 (1981).
15. V. S. Viswanathan, *J. Vac. Sci. Technol.*, 16, 388 (1979).
16. H. W. Lehmann, L. Krausbauer, and R. Widmer, *ibid.*, 14, 281 (1977).
17. J. L. Reynolds, A. R. Neureuther, and W. G. Oldham, *J. Vac. Sci. Technol.*, 16, 1772 (1979); C. H. Ting and A. R. Neureuther, *Solid-State Technol.*, 115 (1982); Y. Sakai, J. L. Reynolds, and A. R. Neureuther, *This Journal*, 131, 627 (1984).

18. R. B. Comizzoli, *RCA Rev.*, **37**, 473 (1976); *This Journal*, **123**, 386 (1976).
19. H. S. Carslaw and J. C. Jaeger, in "Conduction of Heat in Solids," 2nd ed., Clarendon Press, Oxford (1959).
20. M. Yoshizawa, M. Miyake, H. Harado, K. Kiuchi, and S. Tazawa, *This Journal*, **132**, 680 (1985).
21. D. J. Economou, Ph.D. Thesis, University of Illinois (1986).
22. D. Economou, D. Evans, and R. Alkire, Submitted to *This Journal*.
23. D. J. Economou and R. C. Alkire, In preparation.
24. J. A. Liggett and P. L.-F. Liu, "The Boundary Integral Equation Method for Porous Media Flow," George Allen and Unwin, London (1983).
25. S. W. Pang, J. N. Randall, and M. W. Geis, *J. Vac. Sci. Technol.*, **B4**, 341 (1986).

## In and Ex Situ Emission Mössbauer Spectra of No-Carrier-Added $^{119}\text{Sb}$ Electrodeposited on Gold

S. Ambe, T. Okada, and F. Ambe

*The Institute of Physical and Chemical Research (RIKEN), Wako-shi, Saitama 351-01, Japan*

I. Tanaka, S. Nasu, and F. E. Fujita

*Department of Material Physics, Osaka University, Toyonaka-shi, Osaka 560, Japan*

### ABSTRACT

No-carrier-added  $^{119}\text{Sb}$  has been efficiently electrodeposited on a gold foil from a  $0.12 \text{ mol dm}^{-3} \text{ Li}_2\text{SO}_4$  solution of pH 1.5. *In* and *ex situ* emission Mössbauer spectra of the  $^{119}\text{Sb}$  arising from  $^{119}\text{Sb}$  on the gold electrode were measured. Both the *in situ* and *ex situ* spectra consist of two peaks ascribable to isolated single  $^{119}\text{Sb}$  atoms on the surface of gold foil and  $^{119}\text{Sb}$  in antimony metal aggregates, respectively. The two forms of  $^{119}\text{Sb}$  on dried gold are chemically stable against oxidation by air, while partial oxidation occurs by treatment with water.

Electrodeposition of macroamounts of antimony has been extensively studied using various electrolytes (1). While a few hundred mg of antimony was reported to be quantitatively electrodeposited from a mixture of HCl and  $\text{H}_2\text{SO}_4$  solutions (2), electrodeposition yield was only 40-80% from HCl solutions containing 15-60  $\mu\text{g}$  of antimony (3). In electrodeposition of  $^{122}\text{Sb}$  from a  $0.1 \text{ mol dm}^{-3}$  HCl solution for preparation of a thin radioactive source, the yield was as low as 25% (4). These reports indicate that the electrodeposition yield is greatly affected by the amount or concentration of antimony. In electrolysis of microamounts of antimony, it was pointed out that the electrodeposited material was partly redissolved by washing with water (3). The redissolution of electrodeposit by washing is a serious problem in preparation of thin radioactive sources in general. In relation to these problems, it is not only interesting but also important to clarify the chemical states of a microamount of antimony electrodeposited on metal surfaces.

Mössbauer spectroscopy has been successfully used for characterization of electrodeposited layers of iron, cobalt, and tin on a variety of substrates. As early as 1965, Bowles and Cranshaw reported Mössbauer spectra of monolayers of tin formed on a platinum electrode (5). A number of studies have been since performed on dried surface layers of iron, cobalt, and tin which had been electrodeposited before the measurement (*ex situ* studies) (6-9). In a few cases, *in situ* Mössbauer measurement has been applied to electrode surfaces in the process of deposition (10-11). Recently, van Noort *et al.* reported an *in situ*  $^{119}\text{Sn}$  conversion electron Mössbauer experiment, in which a surface layer with a thickness of about 1  $\mu\text{m}$  was measured (12).

In this paper, we describe a high yield electrodeposition method of no-carrier-added  $^{119}\text{Sb}$  on a gold foil and the chemical states of the electrodeposited  $^{119}\text{Sb}$  studied by *in situ* (5, 10) and *ex situ* emission Mössbauer spectroscopy. This technique provides us information on chemical states of single decaying atoms and their surroundings. Mössbauer analysis is made on the 23.9 keV  $\gamma$ -rays emitted by  $^{119}\text{Sn}$  nuclei in the first nuclear excited state ( $^{119}\text{Sn}^*$ , half-life: 17.8 ns) arising from  $^{119}\text{Sb}$  (half-life: 38.0h) by the EC decay. The information furnished by the resonant  $\gamma$ -rays from  $^{119}\text{Sn}^*$  can be utilized to determine the chemical state of  $^{119}\text{Sb}$  before the EC decay, since the Mössbauer

$\gamma$ -ray is emitted immediately (25.7 ns on average) after the decay of  $^{119}\text{Sb}$ , the recoil energy associated with the decay of  $^{119}\text{Sb}$  is much smaller than the displacement energy in solid (13), and the after effects of the decay are negligible in metallic media. The  $^{119}\text{Sb}$  ions in the electrolyte solution are insensitive to Mössbauer measurement.

The gold foil with electrodeposited  $^{119}\text{Sb}$  was used for the study of quenched-in vacancies in gold (14).

### Experimental

No-carrier-added  $^{119}\text{Sb}$  was separated from  $^{119\text{m}}\text{Te}$  (half-life 4.68 days) produced by  $\alpha$ -particle irradiation of tin using the RIKEN cyclotron at our institute. The  $^{119}\text{Sb}$  ions in a  $0.5 \text{ mol dm}^{-3} \text{ LiOH}$  aqueous solution were oxidized to the pentavalent state by air bubbling. The  $^{119}\text{Sb(V)}$  solution was neutralized with  $0.25 \text{ mol dm}^{-3} \text{ H}_2\text{SO}_4$  to pH 6 and was passed through a column filled with activated carbon to remove trace Sn(IV) impurity (15).

The no-carrier-added  $^{119}\text{Sb}$  was electrodeposited on a gold foil cathode (10  $\mu\text{m}$  thick, 18 mm in diam) from  $30 \text{ cm}^3$  of a  $0.12 \text{ mol dm}^{-3} \text{ Li}_2\text{SO}_4$  solution at pH 1-12 using the spiral platinum wire as an anode and applying 10V between the electrodes. The distance between the electrodes was about 2 cm. The electrolyte was stirred continuously by nitrogen gas bubbling during the deposition. The temperature of the electrolyte solution was 50°-60°C during the deposition.

Emission Mössbauer spectra of  $^{119}\text{Sn} \leftarrow ^{119}\text{Sb}$  electrodeposited on a gold foil from a  $0.12 \text{ mol dm}^{-3} \text{ Li}_2\text{SO}_4$  solution of pH 1.5 at  $328 \pm 5 \text{ K}$  under a potential of 10V were recorded by means of conventional Mössbauer spectrometers (Austin S-600 and Ranger 700 Series) using a  $\text{BaSnO}_3$  (0.9 mg  $^{119}\text{Sn cm}^{-2}$ ) absorber kept at room temperature. The 23.9 keV  $\gamma$ -rays were detected using a 2 mm thick NaI scintillation counter with a palladium critical absorber for Sn x-rays. In case of *in situ* measurement, the resonant  $\gamma$ -rays emerging from the back of the gold foil electrode were analyzed in the course of the electrodeposition under potential with the absorber connected to the transducer in parabolic motion. The measurement was usually continued for a few days. At the end of the measurement about 90% of  $^{119}\text{Sb}$  was found on the gold cathode. After the electrodeposition, the aqueous electrolyte